



# Tandem aberration correction optics (TACO) in wide-field structured illumination microscopy

DAOZHENG GONG<sup>1,2</sup> AND NORBERT F. SCHERER<sup>2,3,4,\*</sup>

<sup>1</sup>Graduate Program in Biophysical Sciences, University of Chicago, Chicago, IL 60637, USA

<sup>2</sup>Institute for Biophysical Dynamics, University of Chicago, Chicago, IL 60637, USA

<sup>3</sup>Department of Chemistry, University of Chicago, Chicago, IL 60637, USA

<sup>4</sup>James Franck Institute, University of Chicago, Chicago, IL 60637, USA

\*nfschere@uchicago.edu

**Abstract:** Structured illumination microscopy (SIM) is a powerful super-resolution imaging technique that uses patterned illumination to down-modulate high spatial-frequency information of samples. However, the presence of spatially-dependent aberrations can severely disrupt the illumination pattern, limiting the quality of SIM imaging. Conventional adaptive optics (AO) techniques that employ wavefront correctors at the pupil plane are not capable of effectively correcting these spatially-dependent aberrations. We introduce the Tandem Aberration Correction Optics (TACO) approach that combines both pupil AO and conjugate AO for aberration correction in SIM. TACO incorporates a deformable mirror (DM) for pupil AO in the detection path to correct for global aberrations, while a spatial light modulator (SLM) is placed at the plane conjugate to the aberration source near the sample plane, termed conjugate AO, to compensate spatially-varying aberrations in the illumination path. Our numerical simulations and experimental results show that the TACO approach can recover the illumination pattern close to an ideal condition, even when severely misshaped by aberrations, resulting in high-quality super-resolution SIM reconstruction. The TACO approach resolves a critical traditional shortcoming of aberration correction for structured illumination. This advance significantly expands the application of SIM imaging in the study of complex, particularly biological, samples and should be effective in other wide-field microscopies.

© 2023 Optica Publishing Group under the terms of the [Optica Open Access Publishing Agreement](#)

## 1. Introduction

Advances in optical microscopy have played a key role in biological science research. More biological features and phenomena have been elucidated with better spatial resolution and techniques [1]. However, the quality of microscopy imaging is often hampered by optical aberration. The associated phase variations in the wavefront of the illumination and emission light from its ideal form arise from multiple factors such as index of refraction variations, sample scattering associated with the intrinsic inhomogeneity of complex biological samples, and misalignment and non-ideality of optics [2]. These aberrations lead to decreased resolution, fidelity, and degraded signal-to-noise ratio (SNR) in microscopy images.

In recent years, adaptive optics (AO) has emerged as a promising approach to mitigate optical aberrations in microscopy [3]. The idea is to add phase modulation opposite to the aberration using wavefront correctors such as deformable mirrors (DM) or spatial light modulators (SLM) [4].

Aberration correction with adaptive optics has been primarily applied to point scanning microscopy, e.g., confocal microscopy [5,6] or multiphoton microscopy [7,8], where a phase modulator is generally placed at the pupil plane, termed pupil AO, to correct aberrations that blur the illumination point and point spread function (PSF) [9]. By contrast, aberration correction for wide-field illumination has been largely overlooked and considered to be of negligible importance because of the simplicity of the illumination at the pupil plane. While this might

be a reasonable assumption for uniform wide-field illumination [3,4], it does not hold true for structured illumination microscopy (SIM), which requires careful consideration of aberration correction beyond just the pupil plane.

SIM is a wide-field super-resolution imaging technique that utilizes patterned illumination (typically sinusoidal patterns) to down-modulate high spatial frequency information of a sample into low-frequency beat patterns, also known as the Moiré effect [10]. High-resolution images can then be reconstructed by extracting high-frequency information from these beat patterns [10,11]. However, the reconstruction process is very sensitive to errors in the patterns [12]. Achieving robust reconstruction with minimal artifacts requires that a high-quality pattern be projected onto the sample.

Despite the aforementioned strict requirement for high-fidelity illumination patterns, SIM has long been considered immune to aberrations [13,14]. However, this assumption is only true if spatially-invariant aberrations are considered. Spherical aberration, astigmatism comma, and others have a global effect on the whole field of view (FOV) and can be represented by simple (e.g. parabolic) phase variation functions at the pupil plane of the optical system [13]. To illustrate, consider a sinusoidal illumination pattern that is formed by the interference of 2 or 3 coherent beams. The optical transfer function (OTF) of the pattern only consists of 2 or 3 wavevectors (points) in the pupil plane, as shown in Fig. 1. For this reason, spatially-invariant aberrations will have a very limited effect on the illumination light, and only cause phase or orientation shifts to the illumination pattern. Consequently, almost all adaptive optics applications in SIM have focused on using pupil AO only in the detection path. Although an AO corrector could be placed at a shared pupil plane of both the illumination and detection path, it essentially has no effect on the illumination pattern and only corrects the detection path [14–19].

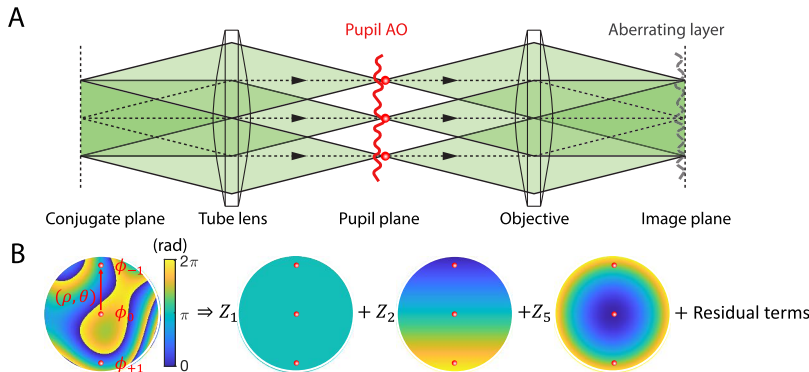


**Fig. 1.** Pupil AO aberration correction for structured illumination. (A) Schematic of the working principle of pupil AO. The wavy red line represents the wavefront modulation at the pupil plane. (B) For 3-beam-interference structured illumination, any phase modulation at the pupil plane can be decomposed into a combination of piston, tilt, and defocus. The residual term has no effect on the illumination pattern. The three red points represent the 3 diffraction-limited spots of the illumination beam(s) at the pupil plane. The phase modulation exerted to the 3 points are denoted by  $\phi_{0,\pm 1}$ . The polar coordinate system of the pupil plane is denoted by  $(\rho, \theta)$ .

However, in biological imaging, the aberrations introduced by the intrinsic heterogeneity of samples can cause severe distortion to a structured illumination pattern. Unlike spatially-invariant aberration, these sample-induced aberrations are spatially varying across the image plane (i.e. sample), and pupil AO can only correct a very limited field of view (FOV) [9,20]. Despite its significance, this spatially-varying source of aberrations has been widely neglected. Clearly, a method to address spatially-varying aberrations in structured illumination is urgently needed.

One approach to address spatially-varying aberration is through conjugate AO [9], which refers to placing an AO corrector at a plane conjugate to the main source of aberration. Doing so directly maps the plane of phase modulation to the aberration plane and allows correcting the entire FOV with a single (but potentially complicated) correction function (see Fig. 2). The advantage of conjugate AO has already been extensively demonstrated [9,21–24]. However, in contrast to pupil AO, conjugate AO cannot compensate for spatially-invariant aberrations such as spherical aberration, which turn out to be the most notorious aberration in the detection path of SIM [15]. For this reason, achieving a fully aberration-corrected SIM system would be best achieved with a *tandem* aberration correction that combines the advantages of both pupil AO and conjugate AO.

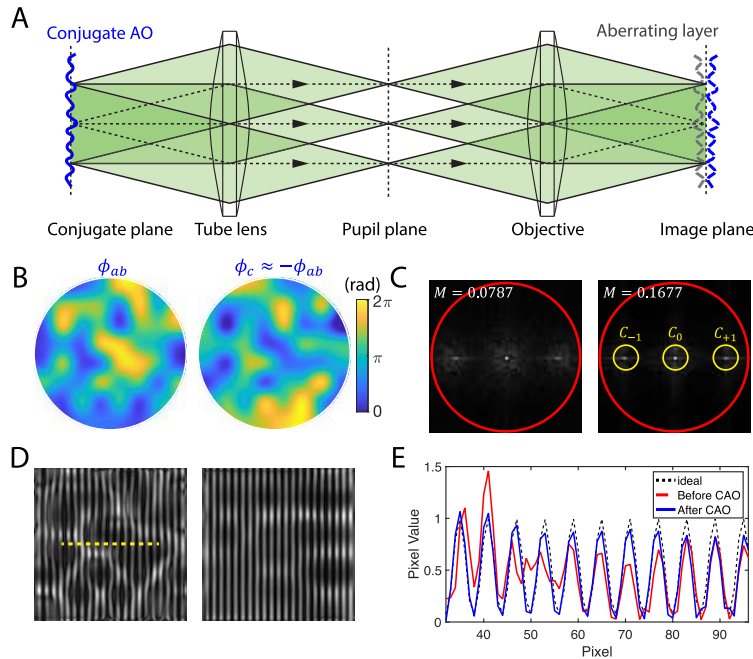


**Fig. 2.** Conjugate AO aberration correction for structured illumination. (A) Schematic of the working principles of conjugate AO. The wavy blue line represents the wavefront modulation at the conjugate plane. (B) The simulated aberration phase mask  $\phi_{ab}(\rho, \theta)$  (left) and the phase correction  $\phi_c(\rho, \theta)$  (right). (C) The simulation results of the FT of the sinusoidal pattern before correction (left) and after correction (right). The yellow circles indicate the sub-images used for calculating the image quality metric  $M$ . The red circle indicates the pupil plane. (D) The simulation results of the sinusoidal pattern (intensity) before correction (left) and after correction (right). (E) The line-cut profile of the cross-section (dashed line) of the pattern in (D) before (red) and after (blue) conjugate AO correction, compared with the profile of an ideal pattern (dashed) without aberration.

In this paper, we present a SIM microscope integrated with a novel Tandem Aberration Correction Optics (TACO) system that uses conjugate AO and pupil AO in the illumination path and detection path, respectively. A DM is used for conventional pupil AO in the detection path to correct for global aberrations, while a SLM is used to implement conjugate AO to compensate for local (spatially-varying) aberration in the illumination beam at the image plane. We demonstrate the effectiveness of our system on uniform fluorescent samples, fluorescent bead monolayers, and cell samples. Our results show that even in the presence of strong aberrations, our TACO

system can robustly correct aberrations and greatly enhance the quality of super-resolution reconstruction.

## 2. Adaptive optics for spatially-varying aberration of structured illumination

Consider the structured illumination formed by 3-beam interference, which is a configuration commonly used for super-resolution SIM imaging with optical sectioning [11]. At the pupil plane, the illumination will form 3 diffraction-limited spots located at the center (0 order,  $\rho = 0$ ) and periphery ( $\pm 1$  orders,  $\rho = \rho_0, \theta = \theta_0, \theta_0 + \pi$ ) as shown in Fig. 1. Then after the objective, the three beams merge, interfere at the image (i.e., focal) plane, and form the periodic illumination pattern. In this process, the beams can be severely affected if traveling through a highly aberrating medium before reaching the image plane (Fig. 1(A)).

If pupil AO was adopted, in which case a wavefront corrector (e.g., a SLM or a DM) is introduced for phase modulation at the pupil plane, then only those SLM pixels or DM segments that co-locate with the diffraction spots affect the phase modulation and the illumination pattern. However, the finite size of the SLM pixel or small local deformation of a DM results in essentially a constant phase modulation being applied to each diffraction order ( $\phi_{0,\pm 1}$ ). Therefore, any phase modulation  $\phi_p(\rho, \theta)$  applied to the pupil can be decomposed into the following form:

$$\phi_p = \frac{\phi_{-1} + 2\phi_0 + \phi_{+1}}{4} + \frac{\phi_{-1} - \phi_{+1}}{2} \frac{\rho}{\rho_0} \cos(\theta - \theta_0) + \frac{\phi_{-1} - 2\phi_0 + \phi_{+1}}{4} \left(2\left(\frac{\rho}{\rho_0}\right)^2 - 1\right) + \text{res} \quad (1)$$

where the first three terms are known as the piston, tilt, and defocus Zernike modes [25]. The combination of these three modes has the same effect on the illumination pattern as the original phase modulation  $\phi_p(\rho, \theta)$  to the 3 diffraction-limited spots, and the residual terms can be neglected (Fig. 1(B)). However, the effect of these three modes on the illumination pattern is trivial: they simply lead to a phase shift or orientation shift of the interference pattern [13,26]. Consequently, pupil AO can exert almost no effective pre-compensation to the illumination pattern to counteract subsequent distortion.

On the other hand, conjugate AO can address this problem rather straightforwardly. Consider a single aberrating layer with phase modulation  $\phi_{ab}(\rho, \theta)$ : conjugate AO employs a wavefront corrector placed in a plane conjugate with the aberrating layer to which one applies an opposite phase modulation of  $\phi_c(\rho, \theta) = -\phi_{ab}$  and hence pre-compensate the illumination beam. In an ideal situation, the phase disruption from each small subregion of the aberration layer will be canceled out by the exact opposite phase modulation from the corresponding area of the wavefront corrector as shown in Fig. 2(A&B). However, in practice, there are factors that limit the efficacy of conjugate AO. Firstly, the aberration may not arise from a single well-defined layer, which creates ambiguity regarding the optimal location of the wavefront corrector. In the case of a thick aberration sample, multiple conjugate AOs [23,27,28], or conjugate AO with a refocusing system [29], might need to be adopted. Secondly, the aberration  $\phi_{ab}$  is usually unknown, and one needs to either directly measure it with a wavefront sensor [21], or optimize the AO phase mask in an iterative manner using an image quality metric (e.g., image contrast) that can be maximized or minimized [9]. In this paper, we confine our discussion to the case of a single aberration layer from a scattering slide, but the TACO concept can be expanded to the case of multiple or thick aberration layers. We chose an image-based iteration method to avoid adding extra complexity to the optical apparatus. The image quality metric is defined as:

$$M = \frac{\sqrt{C_{-1}(w) \cdot C_{+1}(w)}}{C_0(w)} \quad (2)$$

where  $C$  is the contrast (here defined as the standard deviation) of the sub-images around diffraction spots of the FT of a raw image and  $w$  is a user-defined window to adjust the size

of the sub-images (Fig. 2(C)). The contrast of the  $\pm 1$  pattern modulation spatial frequency wavevectors,  $C_{\pm 1}$ , serve as a criterion to allow quantifying the fidelity of the sinusoidal pattern. The 0-order spatial frequency feature,  $C_0$ , in the denominator serves as a normalization to exclude the erroneous solution of increasing the overall brightness of the whole image.

To test the validity of the image quality metric  $M$ , we simulated conjugate AO correction for SIM illumination. A random phase mask was introduced near the image plane of a 4-f imaging system [30] to cause aberration, and the phase modulation was iteratively updated at the conjugate plane to counteract the aberration by maximizing the value of the metric as shown in Eq. (2). The iteration method is based on a stochastic parallel gradient descent (SPGD) algorithm [31,32]. During each iteration, small random perturbations are applied to the phase mask that causes a change of the metric value of  $\delta M$ . The phase mask is subsequently updated using  $\delta M$  as an estimation for the average gradient of  $M$  versus the phase mask values. The details of the algorithm are provided in the [Supplement 1](#). The value of the metric of the initial pattern is 0.0787. After 500 iterations, the metric value converged to a value of 0.1677 (Figure S1). The resulting phase modulation,  $\phi_c$ , at the conjugate plane shows a complementary distribution compared to aberration  $\phi_{ab}$  as shown in Fig. 2(B), which indicates that most of the spatially-varying aberration has been canceled out by conjugate AO. After correction, the first-order spot of the Fourier Transform (FT) of the pattern shows a  $\sim 1.5\times$  increase of intensity versus no correction, while the zero-order spot remains the same (Fig. 2(C)). Figures 2(D & E) show the intensity of the pattern before and after AO correction. Although the pattern has initially been severely distorted by phase aberration, the conjugate AO approach just declared has almost completely compensated the aberration such that the fidelity of the modulation is almost identical to the ideal sinusoidal unaberrated pattern.

### 3. Experimental method

#### 3.1. Microscopy setup

We built a structured illumination microscope (SIM) integrated with a TACO system to illustrate the comprehensive aberration correction capability. An illustration of the TACO-SIM optical setup is shown in Fig. 3(A). A 3-dimensional rendering that closely resembles the actual apparatus is shown in Fig. 3(B).

A solid-state CW laser (Millennia Vs, Spectra Physics, 532 nm, 5-watt maximum power) was used as an illumination light source. The intensity and polarization of the laser beam are controlled by a pair of linear polarizers (P1, P2) and a half-wave plate (HWP1). The laser light passes through a  $4\times$  beam expander formed by a pair of achromatic lenses (L1, L2). A diamond pinhole was placed at the focus to clean the beam profile. A spatial light modulator (Hamamatsu LCOS-SLM X10468) was used for wavefront correction in the illumination path. We used a SLM instead of a DM to allow very detailed phase information to be encoded in the  $800 \times 600$  18-bit pixels of the SLM compared to a deformable mirror (<100 piezo actuators), which allows much more exquisite wavefront modulation to compensate for spatially-varying aberrations. The coherent beam reflected from the SLM is relayed to a digital micromirror device (Texas instrument, DLP9000X VIS WQXGA) by a pair of lenses with  $4\times$  magnification (L3, L4) to cover the entire size of the DMD. The digital micromirror device (DMD) and its corresponding controller board (Digital Light Innovations DLP V4390) were used to generate the structured illumination patterns (see Figure S2). The DMD is rotated  $45^\circ$  in order to make the input and output beams lie in a common horizontal plane. A detailed description of the optical setup of the DMD is provided in the [Supplement 1](#). The 3 diffraction beams resulting from the DMD are imaged to the back focal plane of the tube lens (L7) by a pair of relay lenses with  $5/4\times$  magnification (L5, L6). A half-wave plate (HWP2) mounted on a piezo rotation stage (Newport AG-PR100) is placed at the focal plane to adjust the polarization of the beams in order to maximize the interference contrast, [33]. An optical aberration slide (OAS) is placed at the

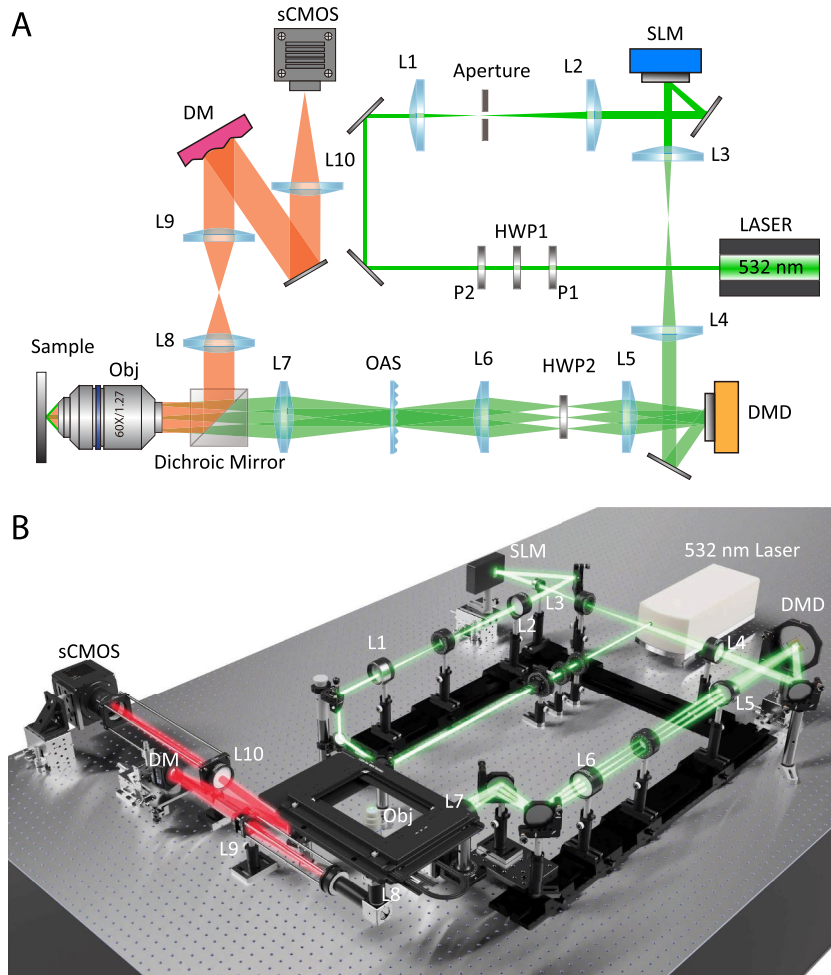


**Fig. 3.** Optical (hardware) setup of the TACO-SIM system. (A) Schematic representation of the microscopy hardware setup. HWP1-HWP2, half-wave plate; DM, P1-P2, linear polarizers. OAS, optical aberration slide; Obj, objective lens; L1-L10, lenses. Lens focal lengths: f1 = 100 mm, f2 = 400 mm, f3 = 100 mm, f4 = 400 mm, f5 = 200 mm, f6 = 250 mm, f7 = 300 mm, f8 = 200 mm, f9 = 200 mm and f10 = 400 mm. (B) 3D rendering of the optical setup. See text for details.

back focal plane of L7 to introduce spatially-varying aberrations in the illumination path. The OAS was made by manually spreading transparent nail polish (Electron Microscopy Science) on a pre-cleaned slide (Fig. S3), which is the same method reported previously [34]. After propagating through the OAS, the now aberrated 3 coherent diffraction beams are directed to the backport of a Nikon Ti Eclipse microscope body, focused by L7 to the pupil plane (back aperture) of the objective (SR Plan Apo, 60×, 1.27 WI, Nikon), and form an interference pattern at the sample plane. For simplicity of demonstration, the OAS only affects illumination light and the emission light is unaffected, so the SLM and conjugate AO only need to operate in the illumination path to compensate. However, this setup with the OAS already manifests significant disruption of the SIM pattern allowing us to demonstrate the capability of the TACO system. The scheme can be extended to the case when the aberration medium affects both illumination

and emission light by placing a wavefront corrector in (a common image plane shared by) both illumination and emission paths.

A high-speed sCMOS array detector (Photometrics Kinetix, 6.5  $\mu\text{m}$  pixel size) is used to record images. A pair of lenses (L9, L10) with a magnification of 2 $\times$  relay the emission from the output port of the microscope to the detector, hence each pixel in the image corresponds to 54 nm at the sample plane. The reason to have the 2 $\times$  relay lens pair is to magnify the FOV of the 16 mm c-mount output port to fully cover the large 29.4 mm detector sensor. Although the present work does not require his large magnification and small pixel size, full usage of the large sensor size is necessary for our other research that uses the same microscope-detector setup. A deformable mirror (Thorlabs DMH40-P01) was placed at the pupil plane for aberration correction in the detection path. There are several reasons for using a DM instead of a SLM in the detection path. Firstly, fluorescent light is unpolarized, while the SLM only works for light with a certain linear polarization. Secondly, the phase modulation of the SLM (on light) is wavelength-dependent, so a fluorescent sample, which has a broad emission spectrum, will result in chromatic aberration if using a SLM. Thirdly, although a DM has less detailed phase modulation capacity compared to an SLM, it is sufficient for global aberration correction at the pupil plane. Finally, the update rate of the DM (4 kHz) is much higher than any SLM (e.g., 60 Hz), allowing additional functions such as high-speed focal plane scanning along the z-axis by changing the curvature of the DM to defocus and refocus the emission light.

### 3.2. Tandem Aberration Correction Optics (TACO)

Implementation of the TACO method is conducted in 2 steps. The first is an image-based pupil AO iteration using the DM to correct global aberrations manifest in the detection path. During this process, the DMD is set to present a completely uniform image (i.e., uniform illumination) to enable wide-field imaging without any structured illumination. The deformation (shape) of the DM is defined by a linear combination of the first 15 Zernike polynomials [25]. The iteration is based on the SPGD algorithm ([Supplement 1](#)) and the metric is the contrast of the image.

Here the contrast is defined as the standard deviation  $\sqrt{\frac{1}{N} \sum_i^N (I_i - \bar{I})^2}$  ( $N$ : total number of pixels,  $I_i$ : value of the  $i_{th}$  pixel,  $\bar{I}$ : mean pixel value) of the image. In each iteration step, the Zernike coefficients will be updated to reshape the DM. Figure 4(A) shows a typical AO process of the DM on images of fluorescent beads. The aberration was introduced by the misalignment of optics. At the beginning of the iteration, the image was severely blurred, while an improvement in image quality can be observed (Fig. 4(A), upper) as the DM's shape is adapted to counteract the optical aberration (Fig. 4(A), lower left). It typically takes 50 ~ 100 steps for the image contrast to converge to a plateau (Fig. 4(A), lower right).

The second step is an image-based conjugate AO iteration using the SLM to correct spatially-varying local aberrations of the illumination path. In this step, the DMD is programmed with a binary periodic pattern for structured illumination. The wavefront modulation of the SLM is defined by values of a 600  $\times$  600-pixel array. The metric  $M$  is defined in Eq. (2) and the iteration procedure is based on the SPGD algorithm ([Supplement 1](#)). Before each update, a Gaussian filter with an empirically determined standard deviation (usually ranging from 0.75 to 1.25) is applied to the SLM pixel array in order to match the smoothly varying phase topography of the aberration slide. Theoretically, the phase correction can be achieved by optimizing pixel-by-pixel independently, but this requires many iterations. The use of an appropriate and modest Gaussian kernel substantially reduces the iterations required. For phase modulations out of the 0 – 2 $\pi$  range, the pixel values are wrapped at 2 $\pi$  (pixel value = 224 in our case) to fit in the modulation range of the SLM. The illumination beam propagates through the aberration slide and becomes strongly distorted. Figure 4(B) shows a typical AO iteration process of the SLM on the fluorescent beads images. It can be seen that although the AO correction by the DM enables functional wide-field imaging with uniform illumination, the structured illumination pattern shows severe distortion

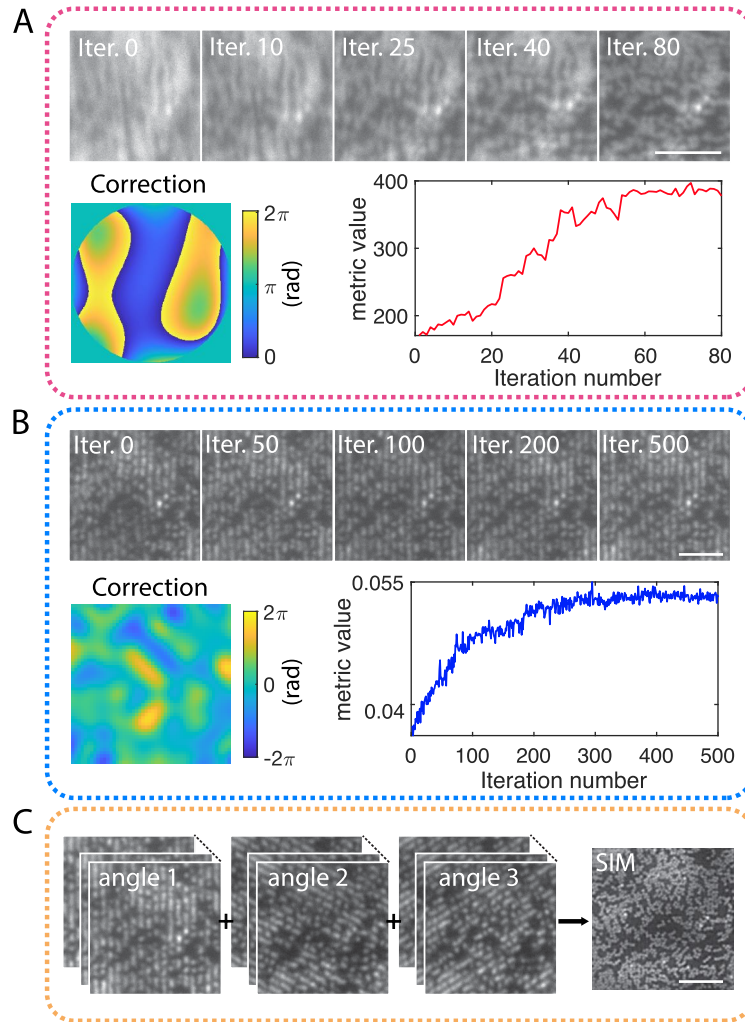


**Fig. 4.** Workflow of the TACO-SIM system. (A) AO iteration process of DM. Upper: Images of fluorescent beads at different iteration steps; Lower left: final wavefront correction pattern of DM; Lower right: the metric value of images versus iteration number. (B) AO iteration process of SLM. Upper: images of fluorescent beads superimposed with a SIM pattern at iteration steps; Lower left: final wavefront correction pattern of SLM. The phase modulation has been unwrapped to better visualize the phase topography; Lower right: the value of the metric of the images versus iteration number. (C) SIM reconstruction from 3 sets of images with SIM patterns at different angles. Scale bars in A, B & C: 4  $\mu\text{m}$ .

resulting from the aberration slide. This distortion was largely rectified (Fig. 4(B), upper) as the SLM updated its pixel array values to compensate the aberration (Fig. 4(B), lower left). Typically it takes 300 ~ 1000 iterations for the metric to converge (Fig. 4(B), lower right).

### 3.3. SIM imaging and reconstruction

We use a series of striped illumination patterns formed by the DMD (Fig. S2) to generate structured illumination. The three-beam interference configuration is employed for its optical sectioning capability [11,35] when imaging 3D samples like cells. The pattern period is 6

pixels and results in an (up to) 85% improvement in resolution with very good pattern contrast maintained. The  $1.85\times$  resolution improvement is determined by both theoretical calculation (Fig. S2) and Fourier ring correlation (FRC) analysis on the experimental images of 20 nm fluorescent bead samples (Fig. S4). Figure 4(C) shows a set of typical SIM raw images and the associated reconstruction result. 18 patterns with 3 angles  $\times$  6 phase shifts are used to create the complete image set required to reconstruct a SIM image. The reason for using 6 phases instead of the conventional 5 phases is to achieve an equidistant phase for the 6-pixel period of the phase patterns. FairSIM, an ImageJ-based open-source SIM reconstruction software [35,36], is used for the reconstruction. Figure 4(C) shows an example of 18 raw images of  $150 \times 150$  pixels reconstructed into super-resolution SIM of  $300 \times 300$  pixels, with each pixel corresponding to 27 nm effective pixel size in the image. Here the relatively small  $150 \times 150$  pixel images shown are purely for display purposes. The other SIM reconstruction images presented in this paper are larger in size. Note that FairSIM uses the OTF attenuation method to retain the optical sectioning ability, which is not a full 3D reconstruction method. More details of the SIM reconstruction are presented in the [Supplement 1](#).

#### 4. Experimental results

The TACO system was first tested on a nearly uniform thin sample layer of carboxylate-modified polystyrene fluorescent beads (Fig. S5). As shown in Figs. 5(A) and 5(B), a SIM pattern without any aberration was imaged, then aberrations were introduced from the aberration slide and also from misalignment of optics. Comparison of Figs. 5(A & B) shows that the sinusoidal pattern was severely distorted by the aberration of the optical beam (Fig. 5(B1)). This is also manifest in the Fourier spectrum since the  $\pm 1$  diffraction orders are barely discernible (Fig. 5(B2)). Figure 5(C) shows the result of only using the DM and pupil AO correction in the detection path. This DM correction resulted in better overall sharpness and contrast in the sinusoidal modulated pattern and its FT (Fig. 5(F)). However, the spatially varying distortion of the pattern still persists. (Note that a spotted grid-like pattern is evident. This results from the SLM pixelation, and also causes the minor diffraction orders in the FTs of the patterns. These grid-like patterns are more obvious when there are spatially varying aberrations present.) To address the spatially-varying aberration, a tandem stage of conjugate AO correction was conducted using the SLM. After 500 iterations, the pattern was restored nearly to the ideal unaberrated quality (Fig. 5(D)). After SLM correction, the profile of the pattern has a shape and contrast close to the ideal undistorted case, which is a significant improvement in comparison with the case of DM-only correction (Fig. 5(E)). The corresponding FTs also show that the diffraction orders following the implementation of TACO become much sharper compared with DM-only correction.

We also tested the same SLM correction on patterns with different orientations as required for SIM reconstruction and found that the quality of all the sinusoidal patterns (i.e., all 3 orientations) were significantly improved (Fig. S6). This observation indicates that the correction is not just limited to a specific pattern orientation. Rather, the wavefront is restored to a plane wave, so optimization of a single SIM pattern gives an overall correction to all the sinusoidal patterns. Doing the SLM correction process based on the image quality of multiple angled patterns can also lead to even more thorough improvement, but comes at the cost of 50-100 additional iterations (Fig. S7).

We tested the quality of SIM reconstruction using images of a sparsely distributed 2D 200 nm dia. fluorescent bead sample. Fig. 6(A) shows a wide-field image of a slide of red fluorescent beads. The 200 nm diameter of the beads is smaller than the resolution of our wide-field microscopy system. The bead sample was illuminated with SIM patterns with different amounts of aberration and different types AO corrections, and reconstructed into the corresponding super-resolved SIM images (Fig. 6(B-F)). In Figure 6(B), the SIM pattern was corrupted by both spatially-varying aberration and global aberration, while no AO correction was performed. The

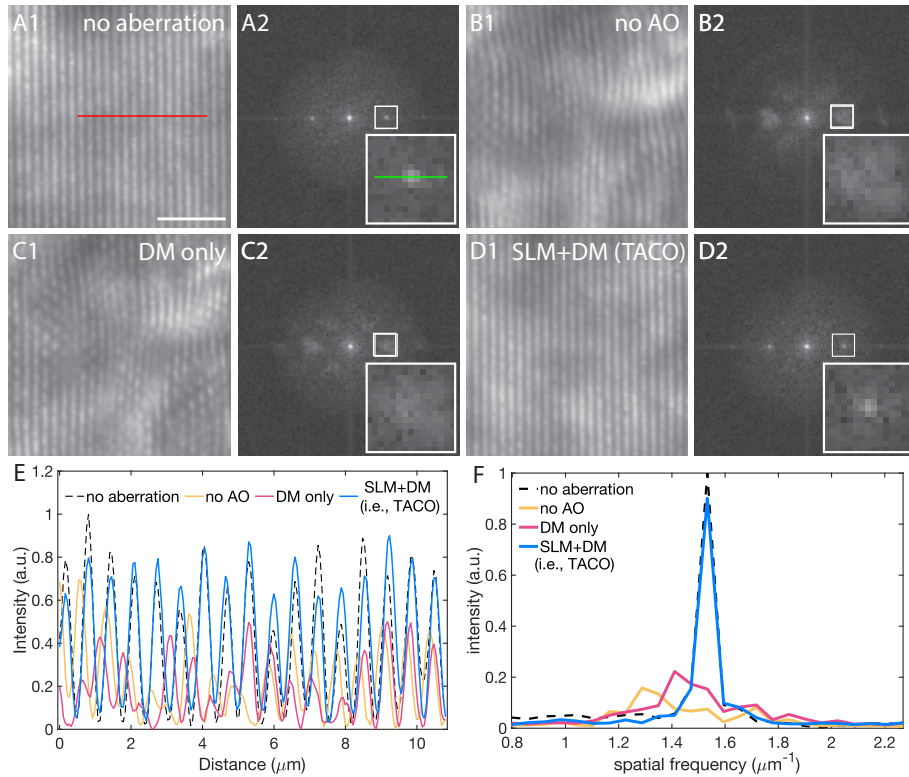


**Fig. 5.** Experimental structured light patterned samples and their Fourier Transforms. (A-D) SIM patterns and associated FT for different conditions. (A1 & A2) no aberration was introduced. (B1 & B2) aberration was introduced both globally and locally. (C1 & C2) Only pupil AO correction by the DM was performed. (D1 & D2) Both conjugate AO by the SLM and pupil AO by the DM were performed, which is the full implementation of TACO. (E) Intensity profile of a cross-section (red line in A1) of the illumination pattern for different conditions. Each curve is smoothed by a moving average with a 3-pixel window and the image background is subtracted to reach the same baseline. (F) Intensity profile of a cross-section (green line in A2) around the first-order spot of FTs for different conditions. To mitigate the edge artifacts, a Gaussian window with a width factor of 0.6% of the image size was applied to the images before doing the Fourier transform. All the FTs have been scaled by a factor of 2, and Gamma corrections are applied with  $\gamma = 0.2$ . Scale bar in A: 5  $\mu\text{m}$ . Effective pixel size: 54nm.

resulting image reconstruction is poor, showing very pronounced artifacts. In Fig. 6(C), only SLM aberration correction for the excitation path was performed, showing some improvement. However, due to the existence of global aberration, the profile of individual beads is still distorted. In Fig. 6(D), only detection path aberration correction was performed using the DM. The quality of reconstruction is spatially-dependent: in some areas, the reconstructed image is free of artifacts and shows good quality (e.g., at the center of the image), while in other areas (e.g., the upper left and lower right parts), the image quality is still severely deteriorated. This result shows how spatially-dependent aberration corrupts image reconstruction in a different way than global aberrations. Finally, Fig. 6(E) shows a substantial improvement with full aberration correction, i.e. implementation of TACO. In Fig. 6(F), no aberration was introduced, and the image was the most ideal. We can see that the image quality after full TACO correction is very close to the ideal unaberrated condition of Fig. 6(F).

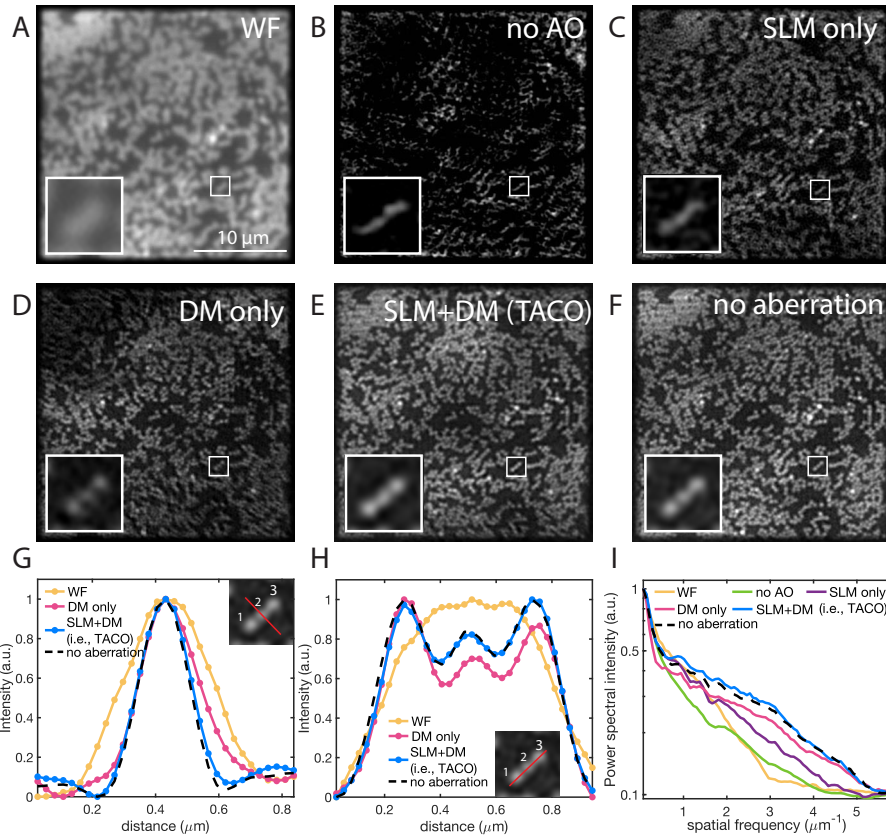


**Fig. 6.** Experimental SIM imaging of 200 nm diameter fluorescent bead sample. (A) Wide-field image of the fluorescent bead sample. (B-F) SIM reconstructed images of the fluorescent bead sample for different aberration correction conditions. (B) No AO correction was performed. (C) Only SLM correction was employed. (D) Only DM correction was employed. (E) Both SLM and DM correction (i.e., TACO) were employed. (F) No aberration was introduced. (G) Normalized intensity profiles along the diagonal cut through bead 2 as shown by the red line in the inset. The profiles of all 3 beads are shown in Fig S7. FWHM values of beads 1-3 are: WF, 343 nm, 331 nm, 327 nm; DM only, 234 nm, 221 nm, 224 nm; SLM+DM, 207 nm, 191 nm, 183nm; no aberration, 190nm, 182 nm, 188nm. (H) Normalized intensity profiles along the diagonal cut through the 3 beads shown by the red line in the inset. The measured distances between the three peaks are: left, 216 nm; right, 243 nm. (I) Power spectrum of images for different conditions. Each curve is normalized by its intensity at zero frequency. Scale bar in A: 10  $\mu\text{m}$ . Effective pixel size: 27 nm.

Fig. 6(G) shows the intensity profile of bead 2 as shown in the inset. The profile shows a clear difference between the different reconstruction strategies. Although DM-only correction shows a much sharper profile (FWHM = 221 nm) compared to WF (FWHM = 331 nm), it is still significantly worse than the no aberration case (FWHM = 182 nm). This can also be seen in the distorted shape of the bead image. On the other hand, TACO correction leads to a further improved bead profile (FWHM = 191 nm) that is very close to the ideal case. Similar results can be seen from the measurements of beads 1 and 3 (Fig. S8A&B). The reason that the FWHM is less than 200 nm might be due to the variance of the manufacturing process. Fig. 6(H) further shows the profiles of the three adjacent beads in the insets. Although the DM-only correction is good enough to show distinguishable profiles of the 3 beads, the profiles of TACO correction

manifest greater fidelity, similar to the unaberrated ideal case. Finally, the power spectra of the images for different imaging and correction conditions are obtained from their FTs (Fig. S9) and shown in Figure 6(I). The y-axis was set to have a log scale to better illustrate the differences between each curve. We also show a linear scale version of the power spectrum analysis in Figure S8D. Compared with the wide-field condition, all the other images show an expansion of the distribution to higher spatial frequency. However, in the case of no AO correction or SLM-only correction, the intensity of high-frequency components is very limited. The case of DM-only correction shows improvement in the high-frequency range but is still inferior to the no-aberration case. By contrast, full implementation of TACO (i.e., both DM and SLM) enhances the frequency distribution to almost the same power spectrum as the ideal case. This further illustrates that the overall quality of the SIM reconstruction after implementing TACO is close to optimum.

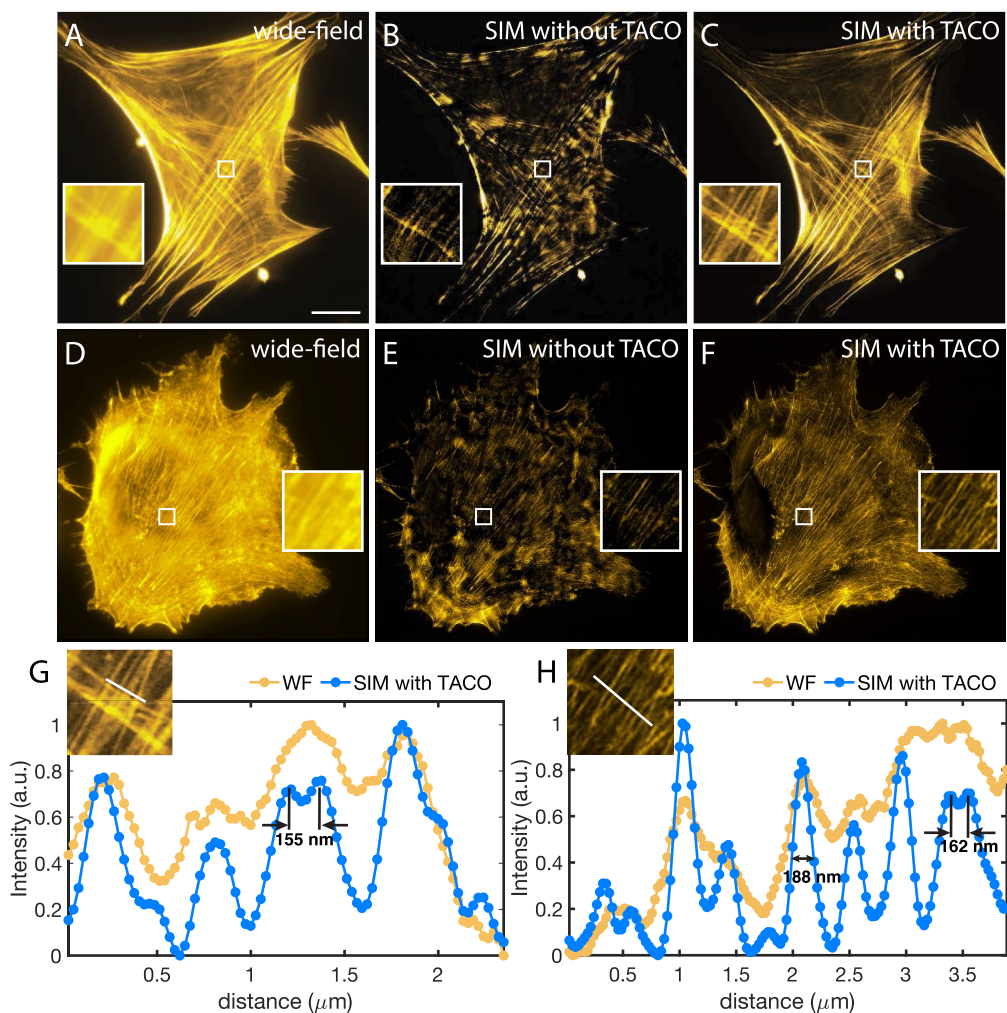


**Fig. 7.** Demonstration of TACO to imaging of phalloidin labeled actin in a human fibroblast cell (upper row) and a human melanoma cell (lower row). (A, D) Wide field images. (B, E) SIM reconstruction without TACO. (C, F) SIM reconstruction with TACO. No additional brightness/contrast adjustment has been added to the images. (H, I) Normalized intensity profile along the lines as shown in the insets. Scale bar in A: 20  $\mu\text{m}$ . Effective pixel size: 27 nm.

#### 4.1. TACO-SIM imaging of biological samples

We further tested TACO aberration correction on two different types of cell samples, human fibroblast cells, and human melanoma cells. We labeled the actin networks of the cells with Alexa Fluor 555 phalloidin fluorescent dye and performed SIM imaging with and without the aberration slide. Wide-field imaging without any introduced aberration was first conducted (Fig. 7(A & D)). The images show poorly-resolved actin structures and strong out-of-focus backgrounds. Figure 7(B & E) show the reconstruction of SIM imaging, including aberration, but without TACO. Due to the strong perturbation from the aberration slide, the SIM pattern was severely distorted (Figure S10A & C) and cannot be reconstructed into accurate super-resolution images. Therefore, one should have low confidence in the cellular features obtained due to the potential artifacts associated with the aberrated illumination patterns. By contrast, the aberration was corrected and the sinusoidal pattern was successfully recovered using TACO (Figure S10B & D), which is what high-quality SIM reconstruction requires. As seen in Fig. 7(C & F), SIM reconstructions after TACO show significantly improved quality, with the artifacts largely eliminated. Compared with wide-field images, the SIM reconstructed super-resolution images show much more detail of the actin networks with improved resolution and contrast and suppression of the out-of-focus light. As shown in 7(G & H), the profile of the actin filaments is significantly more defined after SIM reconstruction with TACO correction; previously indistinguishable actin structures, such as actin branching with separations as small as 155 nm, can be readily resolved.

### 5. Discussion and conclusions

In general, research and application of adaptive optics in SIM have almost exclusively focused on the pupil AO configuration [14–18,37]. However, unlike point-scanning microscopy, wide-field illumination is quite immune to global aberrations like spherical aberration or coma [13,14], but is highly susceptible to spatially-varying aberrations, e.g., caused by sample inhomogeneity or non-flatness of optical components such as DMDs [38]. Consequently, the conventional pupil AO aberration correction approach, which is suitable for the correction of global aberrations but is not able to correct spatially-varying aberrations, is not sufficient for wide-field microscopy techniques such as SIM. In this work, we demonstrated a tandem aberration correction optics - TACO - method to correct both global and local aberrations in SIM.

The present version of TACO incorporates a DM for pupil AO in the optical fluorescence detection path to correct for global aberrations, while a SLM is used for conjugate AO in the optical illumination path to compensate for locally-varying aberrations. We demonstrate that this TACO system is capable of restoring severe SIM pattern distortion, and enables high-quality super-resolution reconstruction that cannot be recovered by pupil AO alone. We note that the main focus of this work is to demonstrate a solution for the long-neglected local aberration lurking in the SIM illumination, instead of the well-studied (both local and global) aberrations in the emission path. Thus the current setup has the conjugate AO only functioning in the illumination path to correct the spatially-varying aberration caused by the optical aberration slide, while for the emission path a basic pupil AO method is adopted. This optical setup can be expanded to allow imaging of thick aberrating samples by adding a conjugate AO corrector in the detection path to further correct for the spatially-variant aberrations in the detection path [21]. Multi-conjugate AO [23,27,28], or refocusing conjugate AO [29] can also be adopted to accommodate a more realistic aberration sample, such as thick biological tissues.

One limitation of the current setup is that the position of the SLM, near the image plane, leads to the projection of its pixelated image onto the sample plane, causing artifacts in the SIM reconstruction. One solution is to use a wavefront modulator with a more continuous wave shaping function, such as a deformable mirror, or a SLM device with a 100% fill factor (e.g. Meadowlark Optics SLM) that does not show observable pixelation. The present experimental advance (TACO) can also be complemented by computational post-processing. Recently, computational

adaptive optics has been shown to compensate aberrations based on purely computational models without the need for wavefront corrector hardware [39,40], providing much more flexibility in the choice of the conjugate plane and AO process. This post-processing approach would complement our hardware-based TACO method.

While we have demonstrated the effectiveness of the TACO approach, we acknowledge that in practical applications, efforts to accelerate the AO correction speed are crucial to enhance the imaging process. For instance, more efficient algorithms like the multidither coherent optical adaptive technique can be employed, which divides the wavefront corrector into independent segments and determines the phase of each segment in parallel [41–43]. Novel devices for direct wavefront sensing have also been designed for large fields of view, such as partitioned aperture wavefront (PAW) sensor [21] and spinning-pupil aberration measurement (SPAM) device [44], which can be used to measure wavefront aberration directly and eliminate the need to do iteration on an image metric.

Overall, the TACO method demonstrates the ability to maintain high-quality SIM illumination and reconstruction when imaging through highly aberrating optical media. Furthermore, the TACO method is not limited to SIM and can also be applied to other novel wide-field microscopy techniques such as multi-color DMD-SIM [45], image scanning microscopy [46,47], multi-plane microscopy [48,49] and temporal focusing microscopy [50]. Furthermore, TACO can be used to correct non-uniformity of the illumination even for conventional wide-field microscopy. Therefore, this method fills a long-standing gap in applying the AO technique to wide-field-based illumination.

TACO should improve wide-field imaging techniques in biological research, especially for imaging through thick tissues, such as brains or embryos, which can cause strong aberration of the illumination light. The TACO system we demonstrate can greatly mitigate this problem and make possible high-quality wide-field illumination patterns. Compared with conventional point scanning microscopy such as confocal and 2-photon, wide-field imaging techniques have the advantage of being able to image the entire FOV at once without the need to scan over the FOV in a time series, and thus could significantly increase the imaging frame rate thereby revealing more details of biological dynamics that were previously inaccessible.

**Funding.** University of Chicago (Grier Award, Institute for Biophysical Dynamics, College Innovation Fund).

**Acknowledgments.** We thank Prof. Jing Chen and Chufan Cai at the University of Chicago for kindly providing the human fibroblast cells and human melanoma cells and for their assistance in cell culture. We thank the University of Chicago, Physical Sciences Division for funds to support this research. We also thank the Institute for Biophysical Dynamics for a Grier Fellowship to D. Gong that also partially supported this research.

**Disclosures.** The authors declare no conflicts of interest.

**Data Availability.** Data underlying the results presented in this paper are not publicly available at this time but may be obtained from the authors upon reasonable request.

**Supplemental document.** See [Supplement 1](#) for supporting content.

## References

1. C. Bond, A. N. Santiago-Ruiz, Q. Tang, and M. Lakadamyali, “Technological advances in super-resolution microscopy to study cellular processes,” *Molecular Cell* **82**(2), 315–332 (2022).
2. K. M. Hampson, R. Turcotte, D. T. Miller, K. Kurokawa, J. R. Males, N. Ji, and M. J. Booth, “Adaptive optics for high-resolution imaging,” *Nat. Rev. Methods Primers* **1**(1), 68 (2021).
3. M. J. Booth, “Adaptive optical microscopy: the ongoing quest for a perfect image,” *Light: Sci. Appl.* **3**(4), e165 (2014).
4. N. Ji, “Adaptive optical fluorescence microscopy,” *Nat. Methods* **14**(4), 374–380 (2017).
5. M. J. Booth, M. A. A. Neil, R. Juškaitis, and T. Wilson, “Adaptive aberration correction in a confocal microscope,” *Proc. Natl. Acad. Sci. U. S. A.* **99**(9), 5788–5792 (2002).
6. X. Tao, B. Fernandez, O. Azucena, M. Fu, D. Garcia, Y. Zuo, D. C. Chen, and J. Kubby, “Adaptive optics confocal microscopy using direct wavefront sensing,” *Opt. Lett.* **36**(7), 1062 (2011).
7. N. Ji, D. E. Milkie, and E. Betzig, “Adaptive optics via pupil segmentation for high-resolution imaging in biological tissues,” *Nat. Methods* **7**(2), 141–147 (2010).

8. K. Wang, D. E. Milkie, A. Saxena, P. Engerer, T. Misgeld, M. E. Bronner, J. Mumm, and E. Betzig, "Rapid adaptive optical recovery of optimal resolution over large volumes," *Nat. Methods* **11**(6), 625–628 (2014).
9. J. Mertz, H. Paudel, and T. G. Bifano, "Field of view advantage of conjugate adaptive optics in microscopy applications," *Appl. Opt.* **54**(11), 3498–3506 (2015).
10. M. G. L. Gustafsson, "Surpassing the lateral resolution limit by a factor of two using structured illumination microscopy," *J. Microsc.* **198**(2), 82–87 (2000).
11. M. G. Gustafsson, L. Shao, P. M. Carlton, C. J. R. Wang, I. N. Golubovskaya, W. Z. Cande, D. A. Agard, and J. W. Sedat, "Three-dimensional resolution doubling in wide-field fluorescence microscopy by structured illumination," *Biophys. J.* **94**(12), 4957–4970 (2008).
12. E. Mudry, K. Belkebir, J. Girard, J. Savatier, E. Le Moal, C. Nicoletti, M. Allain, and A. Sentenac, "Structured illumination microscopy using unknown speckle patterns," *Nat. Photonics* **6**(5), 312–315 (2012).
13. M. Booth, D. Andrade, D. Burke, B. Patton, and M. Zurauskas, "Aberrations and adaptive optics in super-resolution microscopy," *Microscopy* **64**(4), 251–261 (2015).
14. R. Turcotte, Y. Liang, M. Tanimoto, Q. Zhang, Z. Li, M. Koyama, E. Betzig, and N. Ji, "Dynamic super-resolution structured illumination imaging in the living brain," *Proc. Natl. Acad. Sci. U. S. A.* **116**(19), 9586–9591 (2019).
15. M. Arigovindan, J. W. Sedat, and D. A. Agard, "Effect of depth dependent spherical aberrations in 3D structured illumination microscopy," *Opt. Express* **20**(6), 6527–6541 (2012). Publisher: Optica Publishing Group.
16. D. Débarre, E. J. Botcherby, M. J. Booth, and T. Wilson, "Adaptive optics for structured illumination microscopy," *Opt. Express* **16**(13), 9290–9305 (2008). Publisher: Optica Publishing Group.
17. B. Thomas, A. Wolstenholme, S. N. Chaudhari, E. T. Kipreos, and P. Kner, "Enhanced resolution through thick tissue with structured illumination and adaptive optics," *J. Biomed. Opt.* **20**(2), 026006 (2015).
18. Z. Li, Q. Zhang, S.-W. Chou, Z. Newman, R. Turcotte, R. Natan, Q. Dai, E. Y. Isacoff, and N. Ji, "Fast widefield imaging of neuronal structure and function with optical sectioning *in vivo*," *Sci. Adv.* **6**(19), eaaz3870 (2020).
19. R. Lin, E. T. Kipreos, J. Zhu, C. H. Khang, and P. Kner, "Subcellular three-dimensional imaging deep through multicellular thick samples by structured illumination microscopy and adaptive optics," *Nat. Commun.* **12**(1), 3148 (2021).
20. O. Katz, E. Small, and Y. Silberberg, "Looking around corners and through thin turbid layers in real time with scattered incoherent light," *Nat. Photonics* **6**(8), 549–553 (2012). Number: 8 Publisher: Nature Publishing Group.
21. J. Li, D. R. Beaulieu, H. Paudel, R. Barankov, T. G. Bifano, and J. Mertz, "Conjugate adaptive optics in widefield microscopy with an extended-source wavefront sensor," *Optica* **2**(8), 682–688 (2015).
22. J.-H. Park, W. Sun, and M. Cui, "High-resolution *in vivo* imaging of mouse brain through the intact skull," *Proc. Natl. Acad. Sci. U. S. A.* **112**(30), 9236–9241 (2015).
23. T.-W. Wu and M. Cui, "Numerical study of multi-conjugate large area wavefront correction for deep tissue microscopy," *Opt. Express* **23**(6), 7463–7470 (2015).
24. L. V. Amitonova, "Fourier conjugate adaptive optics for deep-tissue large field of view imaging," *Appl. Opt.* **57**(33), 9803–9808 (2018).
25. R. J. Noll, "Zernike polynomials and atmospheric turbulence\*," *J. Opt. Soc. Am.* **66**(3), 207–211 (1976).
26. X. Liu, S. Tu, Y. Xu, H. Song, W. Liu, Q. Liu, C. Kuang, X. Liu, and X. Hao, "Aberrations in structured illumination microscopy: a theoretical analysis," *Front. Phys.* **7**, 254 (2020).
27. P. A. Bedggood, R. Ashman, G. Smith, and A. B. Metha, "Multiconjugate adaptive optics applied to an anatomically accurate human eye model," *Opt. Express* **14**(18), 8019–8030 (2006).
28. R. D. Simmonds and M. J. Booth, "Modelling of multi-conjugate adaptive optics for spatially variant aberrations in microscopy," *J. Opt.* **15**(9), 094010 (2013).
29. X. Tao, T. Lam, B. Zhu, Q. Li, M. R. Reinig, and J. Kubby, "Three-dimensional focusing through scattering media using conjugate adaptive optics with remote focusing (CAORF)," *Opt. Express* **25**(9), 10368–10383 (2017).
30. J. Mertz, *Introduction to Optical Microscopy* (Cambridge University Press, 2019), 2nd edition ed.
31. M. A. Vorontsov and V. P. Sivokon, "Stochastic parallel-gradient-descent technique for high-resolution wave-front phase-distortion correction," *J. Opt. Soc. Am. A* **15**(10), 2745 (1998).
32. B. D. Bing Dong and J. Y. Ji Yu, "Hybrid approach used for extended image-based wavefront sensor-less adaptive optics," *Chin. Opt. Lett.* **13**, 041101 (2015).
33. K. O'Holleran and M. Shaw, "Polarization effects on contrast in structured illumination microscopy," *Opt. Lett.* **37**(22), 4603–4605 (2012).
34. M. Sohmen, J. D. MuPe noz-BolaPe nos, P. Rajaeipour, M. Ritsch-Marte, Ç. Ataman, and A. Jesacher, "Optofluidic adaptive optics in multi-photon microscopy," *Biomed. Opt. Express* **14**(4), 1562–1578 (2023).
35. M. Müller, V. Mönkemöller, S. Hennig, W. Hübner, and T. Huser, "Open-source image reconstruction of super-resolution structured illumination microscopy data in ImageJ," *Nat. Commun.* **7**(1), 10980 (2016).
36. C. A. Schneider, W. S. Rasband, and K. W. Eliceiri, "NIH Image to ImageJ: 25 years of image analysis," *Nat. Methods* **9**(7), 671–675 (2012).
37. H. P. Paudel, J. Taranto, J. Mertz, and T. Bifano, "Axial range of conjugate adaptive optics in two-photon microscopy," *Opt. Express* **23**(16), 20849–20857 (2015).
38. P. T. Brown, R. Kruithoff, G. J. Seedorf, and D. P. Shepherd, "Multicolor structured illumination microscopy and quantitative control of polychromatic light with a digital micromirror device," *Biomed. Opt. Express* **12**(6), 3700–3716 (2021).

39. S. G. Adie, B. W. Graf, A. Ahmad, P. S. Carney, and S. A. Boppart, "Computational adaptive optics for broadband optical interferometric tomography of biological tissue," *Proc. Natl. Acad. Sci. U. S. A.* **109**(19), 7175–7180 (2012).
40. Y. Kwon, J. H. Hong, S. Kang, H. Lee, Y. Jo, K. H. Kim, S. Yoon, and W. Choi, "Computational conjugate adaptive optics microscopy for longitudinal through-skull imaging of cortical myelin," *Nat. Commun.* **14**(1), 105 (2023).
41. M. Cui, "Parallel wavefront optimization method for focusing light through random scattering media," *Opt. Lett.* **36**(6), 870–872 (2011).
42. Q. Zhao, X. Shi, X. Zhu, Y. Zheng, C. Wu, H. Tang, L. Hu, Y. Xue, W. Gong, and K. Si, "Large field of view correction by using conjugate adaptive optics with multiple guide stars," *J. Biophotonics* **12**, e201800225 (2019).
43. R. Liu, D. E. Milkie, A. Kerlin, B. MacLennan, and N. Ji, "Direct phase measurement in zonal wavefront reconstruction using multidither coherent optical adaptive technique," *Opt. Express* **22**(2), 1619–1628 (2014).
44. T. Furieri, D. Ancora, G. Calisesi, S. Morara, A. Bassi, and S. Bonora, "Aberration measurement and correction on a large field of view in fluorescence microscopy," *Biomed. Opt. Express* **13**(1), 262 (2022).
45. D. Gong, C. Cai, S. Eli, J. Chen, and N. F. Scherer, "Easily scalable multi-color DMD-based structured illumination microscopy," Manuscript under review for publication (2023).
46. C. B. Müller and J. Enderlein, "Image scanning microscopy," *Phys. Rev. Lett.* **104**(19), 198101 (2010).
47. A. G. York, S. H. Parekh, D. D. Nogare, R. S. Fischer, K. Temprine, M. Mione, A. B. Chitnis, C. A. Combs, and H. Shroff, "Resolution doubling in live, multicellular organisms via multifocal structured illumination microscopy," *Nat. Methods* **9**(7), 749–754 (2012).
48. S. Xiao, H. Gritton, H.-A. Tseng, D. Zemel, X. Han, and J. Mertz, "High-contrast multifocus microscopy with a single camera and z-splitter prism," *Optica* **7**(11), 1477 (2020).
49. A. Descloux, M. Müller, V. Navikas, A. Markwirth, R. v. d. Eynde, T. Lukes, W. Hübner, T. Lasser, A. Radenovic, P. Dedecker, and T. Huser, "High-speed multiplane structured illumination microscopy of living cells using an image-splitting prism," *Nanophotonics* **9**(1), 143–148 (2020).
50. D. Oron, E. Tal, and Y. Silberberg, "Scanningless depth-resolved microscopy," *Opt. Express* **13**(5), 1468 (2005).